J. Fluid Mech. (1989), *vol.* 203, *pp.* 541–555
Printed in Great Britain

Flow in a partially filled, rotating, tapered cylinder

By R. J. RIBANDO, J. L. PALMER† AND J. E. SCOTT

Department of Mechanical and Aerospace Engineering, School of Engineering and Applied Science, University of Virginia, Charlottesville, VA 22901, USA

(Received 7 January 1988 and in revised form 25 November 1988)

The secondary flow patterns induced by a differentially rotating lid in a partially filled, rapidly rotating, tapered cylinder have been investigated. Using a new laser-Doppler velocimeter system capable of making measurements in the rotor frame of reference, the radial dependence of the azimuthal and axial velocity components was measured at two axial positions in the rotor. A linear, asymptotic analysis and a finite-difference simulation were made for comparison. The latter was performed on a boundary-fitted computational mesh so that the slanted rotor wall and the sagging free surface could be accommodated in the model. The agreement between the experimental and numerical results was excellent for the azimuthal velocity component and good for the axial component. Of particular interest is the modified $E^{\frac{1}{2}}$ boundary layer on the slanted wall, a feature which is not present with a vertical sidewall.

1. Introduction

The flow of a viscous, incompressible fluid in a partially filled, rapidly rotating, tapered cylinder with a differentially rotating lid has been investigated here using analytic, numerical and experimental means. A schematic of the rotor used in this study, including approximate dimensions, is given in figure 1. Typical rotation rates were on the order of 1000 r.p.m., so that the free surface was nearly vertical.

Water mock-up studies such as that reported here have been used to develop concepts and perfect experimental and numerical techniques applicable to gas centrifuges used for uranium enrichment. In this study a new laser velocimeter (LV) system capable of measurements in the rotor frame of reference was developed, and along with a new finite-difference algorithm for strongly rotating flows in non-right circular cylinders, is reported here for the first time.

In a gas centrifuge the heavier $^{238}UF_6$ molecules tend to be concentrated near the periphery while the lighter $^{235}UF_6$ molecules move toward the axis. The imposition of an axial countercurrent flow as studied here (in an incompressible fluid, of course) greatly enhances the separation effect (Hoglund, Shacter & Von Halle 1979; Olander 1972). In a gas centrifuge such secondary flows may be driven thermally; that is, by heating or cooling the side and end walls in some prescribed pattern. Mechanical drives are also used. In the latter case the secondary flow may be driven by the drag of a stationary scoop used for product and/or waste withdrawal or by the insertion or removal of mass. In a water mock-up study, an independently driven endcap provides a convenient means to control the strength of the countercurrent drive. In

† Present address: High Temperature Gas Dynamics Laboratory, Mechanical Engineering Department, Stanford University, Stanford, CA 94305, USA.

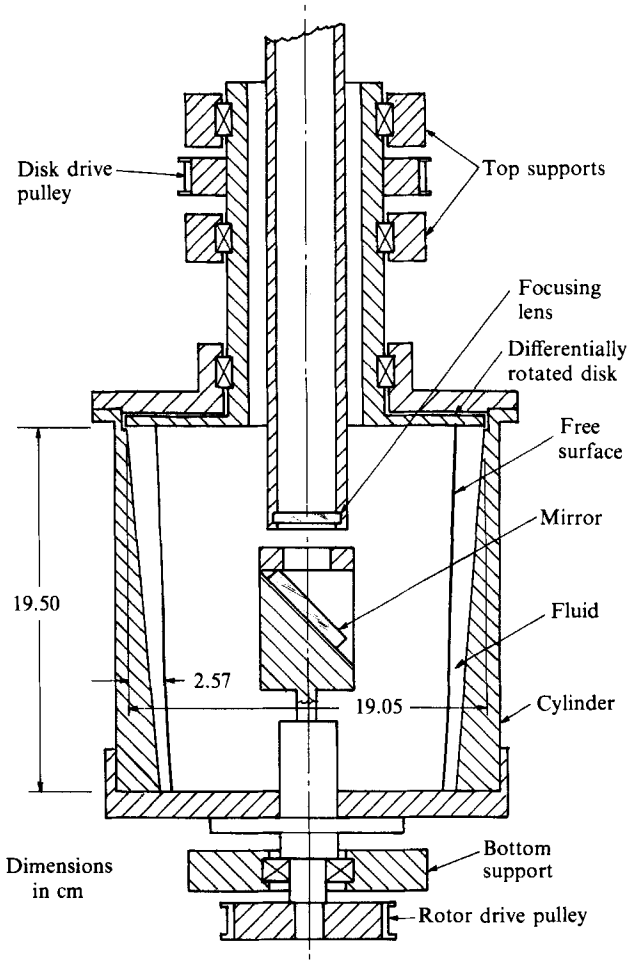

FIGURE 1. Schematic of tapered rotor.

addition the tapered outer wall used in this study provides another possibility for selective tailoring of the strength and pattern of the lid-driven countercurrent flow. A tapered configuration in a gas centrifuge would by itself induce a countercurrent flow because of the density difference between the two isotopes.

Secondary flow patterns in partially filled, rapidly rotating, right circular cylinders have been studied extensively. Shadday (1982) and Beggs (1984) measured the azimuthal and axial velocity profiles in a right circular cylinder with an LV system in the laboratory frame of reference. A theoretical analysis of this flow (Greenspan 1982) was performed concurrently with a numerical investigation (Shadday, Ribando & Kauzlarich 1983; Ribando & Shadday 1984). In particular, Shadday found experimentally and confirmed numerically an unexpected $E^{\frac{1}{3}}$ layer along the free surface. An analysis of this flow has also been given by van Heijst (1986). Smith (1983) measured secondary flows in a tapered cylinder, but too small a taper angle (1.6°) resulted in only minor changes from vertical wall results.

In the current study a 5° wall angle was chosen based on preliminary numerical calculations. The displacement caused by this taper is significant compared to the Stewartson layer thickness, and thus is expected to yield measurable differences from

straight-walled results, but not enough to preclude machining the cylinder wall out of a stock, thick-walled lucite pipe. A new LV system capable of measurements in the reference frame of the rotor (Popp 1987) was designed and is discussed here for the first time. As will be seen, the secondary velocities typically produced by the differentially rotating lid are only of the order of a few percent or less of the solid-body flow. Thus, the possibility of measuring relative to solid-body rather than in the laboratory frame offers the potential for greatly improved accuracy. In addition a new finite-difference simulation was developed using a boundary-fitted coordinate system so that rotating flows in axisymmetric, but otherwise arbitrarily shaped cylinders can be simulated. Here the increased geometric flexibility was used to model the sloped cylinder wall and the parabolic free surface.

A number of parameters characterize this system. Geometric parameters include the aspect ratio, fill ratio, and taper angle of the rotor. Other parameters include the Rossby, Ekman, and Froude numbers, all of which could be easily varied during the course of the experiment. The significance of each will be explained here.

In the absence of differential lid rotation, the flow in the rotor is simply one of solid-body rotation, i.e.

$$\boldsymbol{v}_{\mathrm{sb}} = r\boldsymbol{\Omega}\hat{\theta}. \tag{1.1}$$

The differentially rotating endcap produces a perturbation velocity which is superimposed on the solid-body flow; i.e.

$$\boldsymbol{v} = \boldsymbol{v}_{\mathrm{sb}} + \boldsymbol{v}'. \tag{1.2}$$

Henceforth the velocity will be considered only in a reference frame rotating with the constant angular velocity of the rotor. The velocity of interest is then

$$\boldsymbol{q} = \boldsymbol{v} - \boldsymbol{v}_{\mathrm{sb}} = \boldsymbol{v}'. \tag{1.3}$$

Written in terms of $\boldsymbol{q}$, the continuity and Navier–Stokes equations may be non-dimensionalized and reduced to (Greenspan 1968)

$$\nabla \cdot \boldsymbol{q} = 0, \tag{1.4}$$

$$\frac{\partial \boldsymbol{q}}{\partial t} + \epsilon \boldsymbol{q} \cdot \nabla \boldsymbol{q} + 2\hat{\boldsymbol{k}} \times \boldsymbol{q} = -\nabla p - E\nabla \times (\nabla \times \boldsymbol{q}). \tag{1.5}$$

Here $L\Omega^{-1}, U$, and $p\Omega UL$ have been used to non-dimensionalize r, t, q, and p, the reduced pressure, respectively.

The Rossby number ϵ is seen to measure the relative importance of the convective terms in the Navier–Stokes equations. Here the characteristic velocity U is taken as $(\Omega_{\mathrm{D}} - \Omega)L$, where Ω_{D} refers to the independently driven endcap and Ω to the rotor itself. Then the Rossby number is simply

$$\epsilon = \frac{\Omega_{\mathrm{D}} - \Omega}{\Omega}. \tag{1.6}$$

Values used in the experiments ranged from 0.1 to 0.5.

The Ekman number,

$$E = \nu/\Omega L^2, \tag{1.7}$$

where ν is the fluid kinematic viscosity and L is the container length, measures the importance of viscous forces relative to the Coriolis force. Values used here are typically on the order of 10^{-5} to 10^{-6}. For low values of Ekman number the flow consists of an inviscid interior plus boundary layers of thickness proportional to fractional powers of the Ekman number. On non-vertical surfaces, which here

include the ends and the slanted wall, Ekman layers of thickness of order $E^{\frac{1}{2}}$ form. These layers transport fluid radially and bring about transition between the interior flow, where viscous forces are negligible, and the solid surfaces of the container. At any radius at which a discontinuity in angular and/or axial velocity occurs, Stewartson layers of thickness proportional to $E^{\frac{1}{4}}$ and/or $E^{\frac{1}{3}}$ will form. The $E^{\frac{1}{3}}$ layer serves both to smooth the axial velocity and to transport fluid axially, while the $E^{\frac{1}{4}}$ layer smooths the discontinuity in the angular velocity.

The last parameter, which in solid-body rotation determines the free surface shape, is the Froude number:

$$Fr = \Omega^2 L/g. \tag{1.8}$$

In solid-body rotation the water–air interface is a paraboloid described by

$$z = Fr\,\tfrac{1}{2}r^2 + C. \tag{1.9}$$

The asymptotic analysis of this problem detailed in Palmer (1987) assumes infinite Froude number; that is, a vertical inner boundary. The numerical simulation discussed in the next section uses the shape in solid-body rotation; i.e. the parabola given above as the free surface shape. Under the higher Rossby number conditions ($\epsilon \gtrsim 0.3$) it was possible to see small changes in the free surface shape particularly near the top of the rotor as the disk speed was increased. This effect is not included in the model.

The work of Palmer (1987) assumes that the Ekman number to the fractional powers $\frac{1}{2}$, $\frac{1}{3}$ and $\frac{1}{4}$ and the Rossby number, ϵ, are much smaller than the mean non-dimensional fluid thickness, so that a linearized asymptotic analysis may be performed. The interface between the fluid and the air core is assumed to support no viscous stresses. Details of the solution procedure including the geostrophic flow, Ekman layers on the ends and slanted sidewall and shear layers at the inner free surface and centred on the inner radius of the slanted sidewall may be found in Palmer (1987). The general flow pattern, evaluated using the stream functions thus determined, shows a vortical structure in the meridional plane similar to that computed numerically and displayed later. Of particular interest is the boundary layer on the slanted sidewall, the thickness of which is found to be $(\mathrm{cosec}\,\alpha)^{\frac{1}{2}}E^{\frac{1}{2}}$.

2. Numerical model

In order to simulate the flows for which the measurements reported here were made, a finite-difference model of the linearized governing equations was developed. This model incorporates many of the features of previously reported models for strongly rotating axisymmetric flows (Shadday *et al.* 1983; Ribando & Shadday 1984) but was written here using a boundary-fitted coordinate system. This feature was used to incorporate both the slightly off-vertical free surface and the sloped outer boundary of the cylinder.

The time-dependent linearized, axisymmetric governing equations are written in component form as follows:

$$\frac{\partial u}{\partial t} = 2v - \frac{\partial p}{\partial r} + E\left(\frac{\partial}{\partial r}\frac{1}{r}\frac{\partial}{\partial r}ru + \frac{\partial^2 u}{\partial z^2}\right), \tag{2.1}$$

$$\frac{\partial v}{\partial t} = -2u + E\left(\frac{1}{r^2}\frac{\partial}{\partial r}r^3\frac{\partial v/r}{\partial r} + \frac{\partial^2 v}{\partial z^2}\right), \tag{2.2}$$

$$\frac{\partial w}{\partial t} = -\frac{\partial p}{\partial z} + E\left(\frac{1}{r}\frac{\partial}{\partial r} r \frac{\partial w}{\partial r} + \frac{\partial^2 w}{\partial z^2}\right), \tag{2.3}$$

$$\frac{1}{r}\frac{\partial}{\partial r} ru + \frac{\partial w}{\partial z} = 0. \tag{2.4}$$

These equations must be transformed from the (r, z)-physical domain into the rectangular (η, ξ)-computational plane (Maliska & Raithby 1984; Patel & Briggs 1983; Ostrander 1985). The radial momentum equation is typical:

$$\frac{\partial u}{\partial t} = 2v - \frac{z_\eta}{J}\frac{\partial p}{\partial \xi} + \frac{z_\xi}{J}\frac{\partial p}{\partial \eta} + \frac{E}{J}\left(\frac{\partial}{\partial \xi}\frac{\alpha}{rJ}\frac{\partial}{\partial \xi} ru - \frac{\partial}{\partial \xi}\frac{\beta}{rJ}\frac{\partial}{\partial \eta} ru - \frac{\partial}{\partial \eta}\frac{\beta}{rJ}\frac{\partial}{\partial \xi} ru + \frac{\partial}{\partial \eta}\frac{\gamma}{rJ}\frac{\partial}{\partial \eta} ru\right). \tag{2.5}$$

The continuity equation transforms to

$$\frac{\partial}{\partial \xi} rU + \frac{\partial}{\partial \eta} rW = 0. \tag{2.6}$$

Here, $J = r_\xi z_\eta - r_\eta z_\xi$ and the metrics are related by $\xi_r = z_\eta/J$, $\xi_z = -r_\eta/J$, $\eta_r = -z_\xi/J$, $\eta_z = r_\xi/J$. The coefficients α, β, and γ are equal to $r_\eta^2 + z_\eta^2$, $r_\xi r_\eta + z_\xi z_\eta$, and $r_\xi^2 + z_\xi^2$, respectively, and $U = z_\eta u - r_\eta w$ and $W = r_\xi w - z_\xi u$ are the contravariant velocities.

Equation (2.5), analogous equations for the other velocity components and (2.6) were solved using a primitive variable, time-marching, finite-difference procedure (Harlow & Welch 1965) extended and improved for strongly rotating flows in a manner similar to that discussed in Shadday *et al.* (1984) and still further altered for non-orthogonal meshes following the procedures discussed in Maliska & Raithby (1984).

Because rotating flows support inertial waves which may be excited inadvertently by any source including the truncation error of the finite-differencing (Greenspan 1968; Heuser, Ribando & Wood 1986), and also can be a source of numerical stability problems, all terms in the subset of the above equations which governs inviscid inertial waves were treated in a fully implicit fashion. Thus, in schematic form (2.5) was differenced as

$$\frac{u_{i,j}^{N+1} - u_{i,j}^{N}}{\Delta t} = 2v_{i,j}^{N+1} - \frac{z_\eta}{J}\frac{\partial p^{N+1}}{\partial \xi} + \frac{z_\xi}{J}\frac{\partial p^{N+1}}{\partial \eta} + \text{Viscous}_{i,j}^{N}, \tag{2.7}$$

where the superscripts N and $N+1$ indicate the present and advanced time levels, respectively. The azimuthal and axial equations are differenced similarly.

As in previous work the azimuthal momentum equation is used to eliminate the v^{N+1} in the radial momentum equation. Forms for u^{N+1} and w^{N+1} may then be substituted into the difference form of the continuity equation (2.6) evaluated at the $N+1$ time level to form an elliptic equation for pressure at the new $(N+1)$ time level. The procedure by which two rather than one set of velocity equations are solved per primary (pressure) control volume is discussed extensively in Maliska & Raithby (1984) and used here.

In all of the proceedings it is assumed that the time step Δt is the same for the whole grid. For low-Ekman-number flows, the explicit treatment of the viscous terms used here may lead to excessively small time steps since, in order to resolve the Ekman layers at the ends, one needs a vertical grid spacing on the order of $\frac{1}{4}$ to $\frac{1}{3}$ of the boundary-layer thickness. The current approach is to use a 'skewed' time transient, that is to advance the parabolic velocity equations, e.g. (2.7), at a substantial

fraction of the maximum allowable time step computed locally One other feature which distinguishes the method used here is that for low values of Ekman number ($< 10^{-5}$), where the Taylor–Proudman theorem is approximately valid, only direct methods (Dongarra *et al.* 1979) were found feasible for solving the pressure equation. Long-wavelength errors characteristic of this regime caused iterative methods to be impractical.

The viscous terms are evaluated using centred differences. Slip and no-slip boundary conditions are implemented by reflecting contravariant velocities with appropriate sign and then computing the velocity components from them. The free surface shape is input, and that surface is taken to be impermeable and free slip.

3. Experimental apparatus and procedure

While earlier studies used an LV system fixed in the laboratory frame of reference (Shadday 1982), the system used for this experiment (figure 2) was similar to that of Tokoi, Ozaki & Harada (1980), whose rotating frame of reference, backscatter LV system was used to measure azimuthal and axial velocities in a rapidly rotating gas. The source of the incoming radiation to this system was a Lexel Model 95-4 argon-ion laser operated in its fundamental (TEM_{00}) mode at a wavelength of 514.5 nm and a power of 340 mW. Details of the collection optics and signal processing electronics are given by Beggs (1984) and Popp (1987). As before, the fluid inside the lucite rotor was seeded with neutral-density polystyrene latex particles $1.091 \pm 0.0082\,\mu m$ in diameter (Beggs 1984).

A phase-angle variation between the rotating beam splitter and the rotor was used to measure the axial velocity profiles. This method is illustrated in figure 3. The resulting tilt in the plane formed by the beams from the horizontal is identified as the angle κ. The lens was moved axially to move the probe volume radially between the free surface and the wall. Approximately 575 individual frequency measurements were averaged to obtain the velocity at each of about 60 points in the interval. A total of five similar radial traverses were made to obtain a single set of azimuthal and axial velocity profiles. Initially, the optics angle $\kappa = 0°$ was used to measure the azimuthal velocity. Ideally, the next step would have been to make a radial traverse with $\kappa = 90°$; however, because the azimuthal perturbation velocity is generally an order of magnitude greater than the axial velocity, particles would be swept through the probe volume so quickly that they would not cross enough fringes to create a useful signal. A remedy for this problem, similar to, but not identical with that used by Shadday (1982), involved making two radial traverses of the fluid layer at $\kappa = 72°$ and $-72°$. The axial velocity component could then be determined from these measurements. A second independent measurement of the axial velocity was made with radial traverses at $\kappa = 48°$ and $-48°$, to serve as a verification of the first measurement.

Many sources of small, random errors were present in the LV, system, including variations in the fluid composition and temperature, uncertainties in the rotor and disk speeds, various reflections of laser and ambient light into the photomultiplier tube, etc. Beggs (1984) discussed the sources of error which are pervasive in LV systems of this type, and every attempt was made to minimize these errors. In addition to random error, two important sources of systematic error existed in the LV system used for this study. These errors, specific to and inherent in the rotating reference frame LV system, were caused by slight mechanical misalignments which

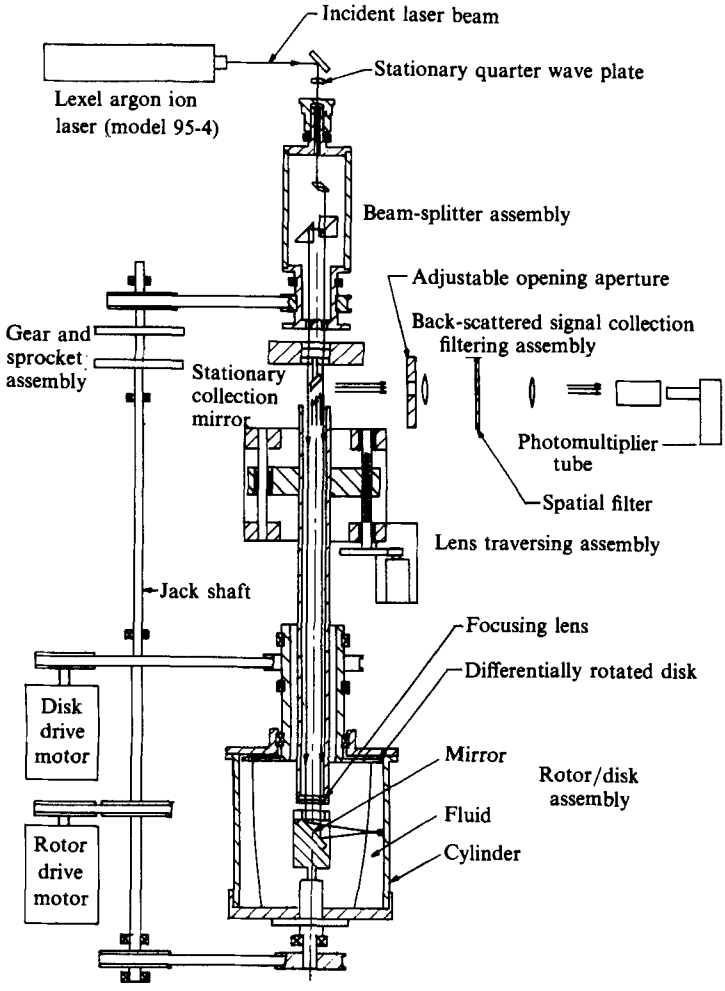

FIGURE 2. Schematic of apparatus showing LV system.

were not present in the laboratory frame of reference system used by Shadday (1982) and Beggs (1984). The first error is the small velocity fluctuation superimposed on the measured velocity in the rotating frame which results from any horizontal displacement or tilt of the focusing lens with respect to the axis of the beam splitter, mirror, and rotor. The misalignment of these axes produced a circular motion of the probe volume in the axial–azimuthal plane in the rotating reference frame. Fortunately, the presence of this misalignment could be monitored during the experiment by examining the signal displayed on an oscilloscope for a sinusoidal pattern. When a fluctuating pattern was detected in the signal, the position of the lens axis was manually adjusted to minimize the fluctuation.

The other systematic error was caused by minor changes in the alignment of the rotor drive system between measurement periods. This resulted in a rotational phase angle between the beam splitter and the rotor slightly different, by an amount κ', from the angle set by the transmitting optics. This small angle, which was consistently on the order of 1°, was constant over the measurement period, but

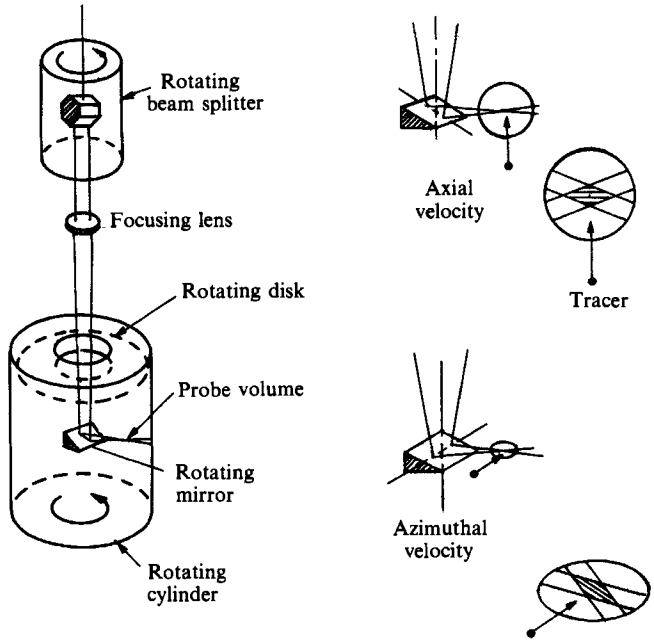

FIGURE 3. Overview of rotating-reference-frame laser velocimeter (Tokoi *et al.* 1980).

varied between periods when the rotor was removed from the system. This improper phase-angle variation was largely eliminated by adjustment of the rotor drive pulley with the optics in the pure azimuthal measurements mode ($\kappa = 0°$) prior to each measurement period. The effect of κ' on the measured velocities was to displace the entire profile by a nearly constant amount dependent on its value.

Locating the probe volume inside the fluid layer was complicated by the three-dimensionality of the refraction which occurs when the laser beams pierce the parabolic free surface. A detailed analysis of the problem is given by Popp (1987). This effect also had to be accounted for in the conversion of Doppler frequency to velocity. Although its size was slightly affected by its location, the ellipsoidal probe volume was approximately 3 mm along its major axis by 1 mm along its minor axis.

Of central importance in this study is the determination of the Ekman number. While Ω and L could be accurately measured, the value of the kinematic viscosity ν was subject to some error. A mixture of distilled water and 75.7% by volume glycerine was used throughout the measurements. During preliminary testing of the LV system, it was found that the fluid temperature varied with the Rossby number. Approximate equilibrium temperatures were obtained for Rossby numbers of 0.10 and 0.50 by monitoring the temperature changes over a 3 h spin period for each Rossby number. Before each test, the fluid was heated in a closed container to the expected equilibrium temperature for the Rossby number to be used. The fluid temperature was recorded after a spin-up and equilibration period of about 1 h, between the five radial traverses made to complete a single set of measurements, and after the entire measurement period. Temperatures ranged from $24.7 \pm 0.5\,°C$ at a Rossby number of 0.1 to $31.7 \pm 1.2\,°C$ at a Rossby number of 0.5.

Preliminary testing under conditions identical with those during the data collection period also revealed that a significant amount of evaporation took place

from the fluid over long spin times, particularly at large Rossby numbers. Since the vapour pressure of glycerine is less than 1% of that of water for the temperature range used in the experiments, a small, empirically determined amount of distilled water was added to the mixture between radial traverses to replace the evaporated amount. Approximately 5 ml of distilled water was added every 3 h. The total fluid volume used in the experimentas was approximately 1770 ml. The fluid thickness at the axial position $z = 0.54L$ was about 2.0 cm; while at the other axial position where data were taken, $z = 0.80L$, the thickness was about 2.3 cm.

4. Results

Measured and numerical results for two cases will be presented here. These included measurements in the slanted-wall rotor and also for a reference straight-wall rotor at similar conditions (Popp 1987). The Rossby number for all cases presented here was 0.10 corresponding to a 10% overspeed, so that the linear finite-difference analysis should be valid for comparison. Measurements were made at Rossby numbers up to 0.50, but those higher Rossby number results will only be discussed in passing. The numerical calculations were run out to 1.5–2.0 times the spin-up timescale ($E^{-\frac{1}{2}}$) based on the time steps away from endwalls. Using a 30×40 mesh, this took between 4 and 5 min of CPU time in the vectorized mode on a Convex C-1 minisupercomputer.

Azimuthal and axial velocity measurements were made at two axial positions along the slanted rotor. Figure 4(*a*) shows an azimuthal velocity traverse at slightly above the midpoint on the rotor for an Ekman number of 9.7×10^{-6}. The radial position has been scaled by the local fluid-layer thickness, so that $\tilde{R} = 0$ corresponds to the free surface and $\tilde{R} = 1.0$ corresponds to the solid wall. Also indicated along the horizontal scale are the distances $E^{\frac{1}{2}}\cos\alpha/(\sin\alpha)^{\frac{1}{2}}$, $E^{\frac{1}{3}}$, and $E^{\frac{1}{4}}$, the characteristic boundary-layer thicknesses anticipated from the analysis. The velocities have been scaled by the peripheral speed of the lid ($\epsilon\Omega R_{\max}$) rather than the original form (ΩL) which was used to non-dimensionalize the governing equations. The approximate absolute velocity in m/s in the rotating frame can be determined by multiplying the dimensionless velocity plotted by 10ϵ ($\epsilon\Omega R_{\max} = \epsilon \times 2\pi \times 16.67$ Hz $\times 9.53$ cm $\approx 10\epsilon$ m/s). Thus the azimuthal values through about 80% of the layer thickness correspond to about 0.2 m/s ($= 10 \times 0.1 \times 0.2$) relative to the rotor. In contrast the rotor peripheral speed is about 10 m/s.

The measured data show little scatter and compare extraordinarily well with the finite-difference predictions (solid line) over the whole range. For comparison a case with a very high Froude number such that the interface was vertical was also modelled; these results are denoted by the dashed line. The effect of the small free surface slope (approximately 1%) on the flow is seen to be substantial. With the vertical free surface the fluid ascends without a radius change. With the slanted free surface the fluid is forced outward where, by conservation of angular momentum, it shows a lower angular velocity than it would otherwise.

Figure 4(*b*) shows a radial traverse of the axial velocity at the same axial position. Agreement between the numerical solution and the experimental results is acceptable, though not as good as for the azimuthal component. The precision of the experimental points is less than for the azimuthal component since these velocities are a full order of magnitude smaller and, as discussed earlier, were measured indirectly. In particular the extremes predicted by the numerical model appear

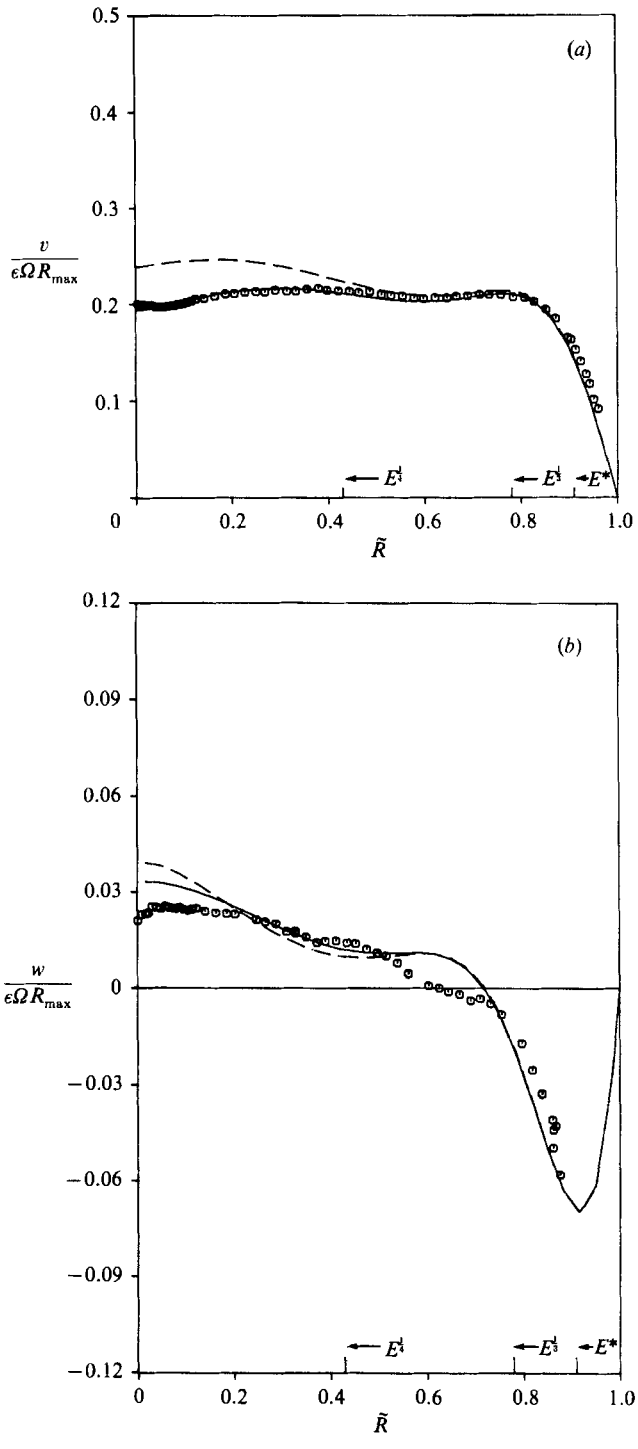

FIGURE 4. Measured and computed traverses at $z = 0.54$ for Ekman number $= 9.7 \times 10^{-6}$, Rossby number $= 0.10$. Experimental data indicated by symbols; solid line indicates computed results at actual Froude number (218); dashed line indicates computed results at Froude Number of 10^5. Characteristic layer thicknesses are indicated on the abscissa. Here E^* stands for $E^{\frac{1}{2}} \cos\alpha (\operatorname{cosec}\alpha)^{\frac{1}{2}}$. (*a*) Azimuthal velocity, (*b*) axial velocity.

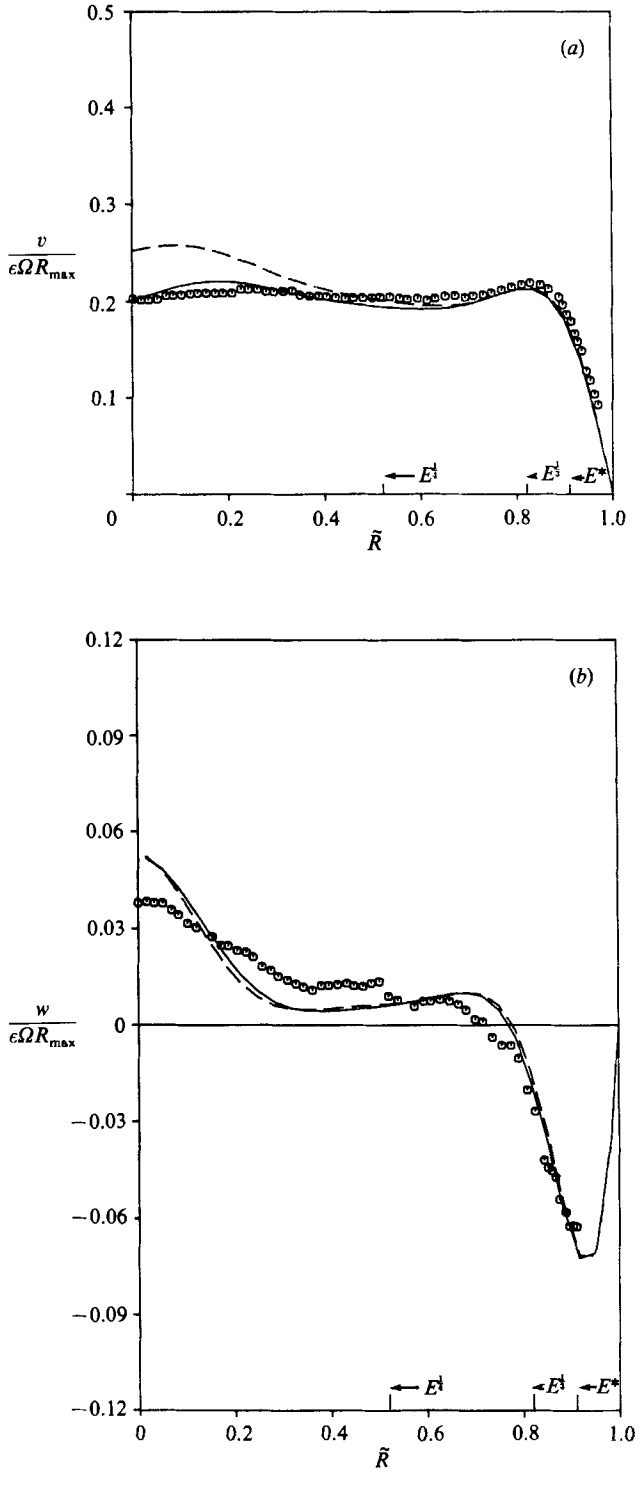

FIGURE 5. Results for same parameters as in figure 4, but at $z = 0.80$. (*a*) Azimuthal velocity, (*b*) axial velocity.

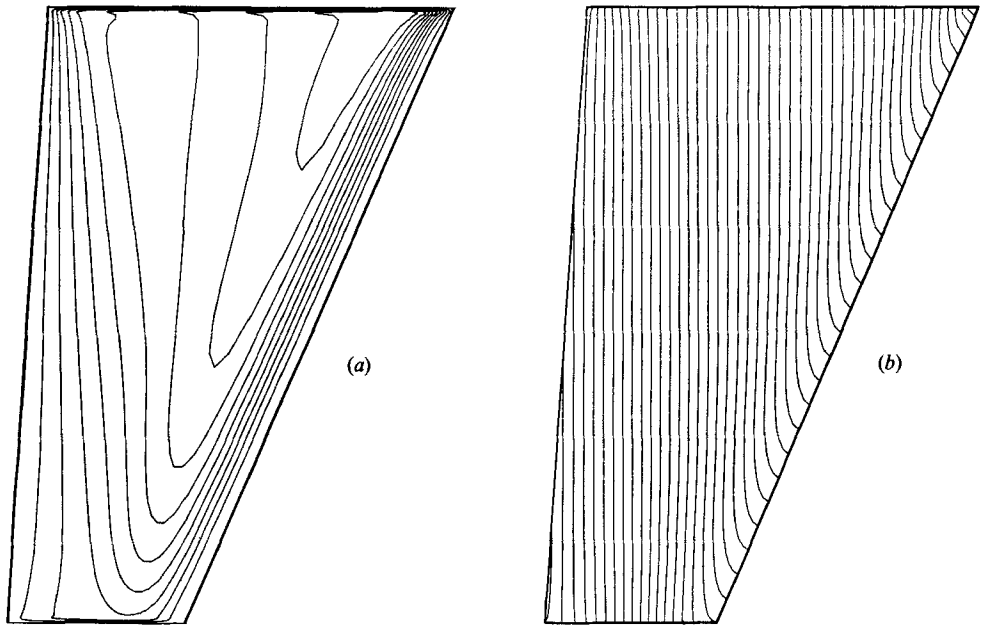

FIGURE 6. Computed streamlines (*a*) and isobars (*b*) for $E = 9.7 \times 10^{-6}$. Horizontal scale has been expanded by a factor of 5.0.

attenuated in the laboratory data. Again the finite-difference results at the actual Froude numer of 218 show better agreement through the inner half of the layer than do the infinite-Froude-number results.

Results with the same parameters but at the other axial station ($z = 0.80$) are plotted in figure 5(*a*, *b*). Here the characteristic layer thicknesses marked on the abscissa appear less than at the other station; this is simply a result of the layer thickness being greater higher up in the cylinder. Significantly higher axial velocities are found in both numerical and measured velocities at the free surface than at the other measuring position. Agreement here is not as good as farther down the rotor. One explanation is that near the top of the rotor the deviation in shape of the free surface from the assumed paraboloid is beginning to become important. Plots of the computed stream function (figure 6*a*) and isobars (figure 6*b*), both of which were expanded by a factor of five in the radial direction, lend some insight. The streamlines along the free surface near the upper lid clearly show a convergence corresponding to the higher-than-measured axial velocities. The isobar plot is more revealing. Outside the boundary layer on the slanted sidewall, the Taylor–Proudman theorem is seen to be operative; i.e. the isobars show little variation with altitude. It is also apparent why solving the pressure equation by a pointwise iterative procedure is not feasible. More importantly several isobars are seen to intersect the free surface. The surface was modelled as being free of viscous stress, but was taken as impermeable with the solid-body-rotation shape. Thus, a non-zero surface pressure is possible. If the actual distorted free surface shape (corresponding to the non-zero Rossby number) had been known and used rather than the parabola, then presumably the free surface would have been found to be both a zero pressure and impermeable boundary.

Both measured and computed results for similar parameters in a straght-walled

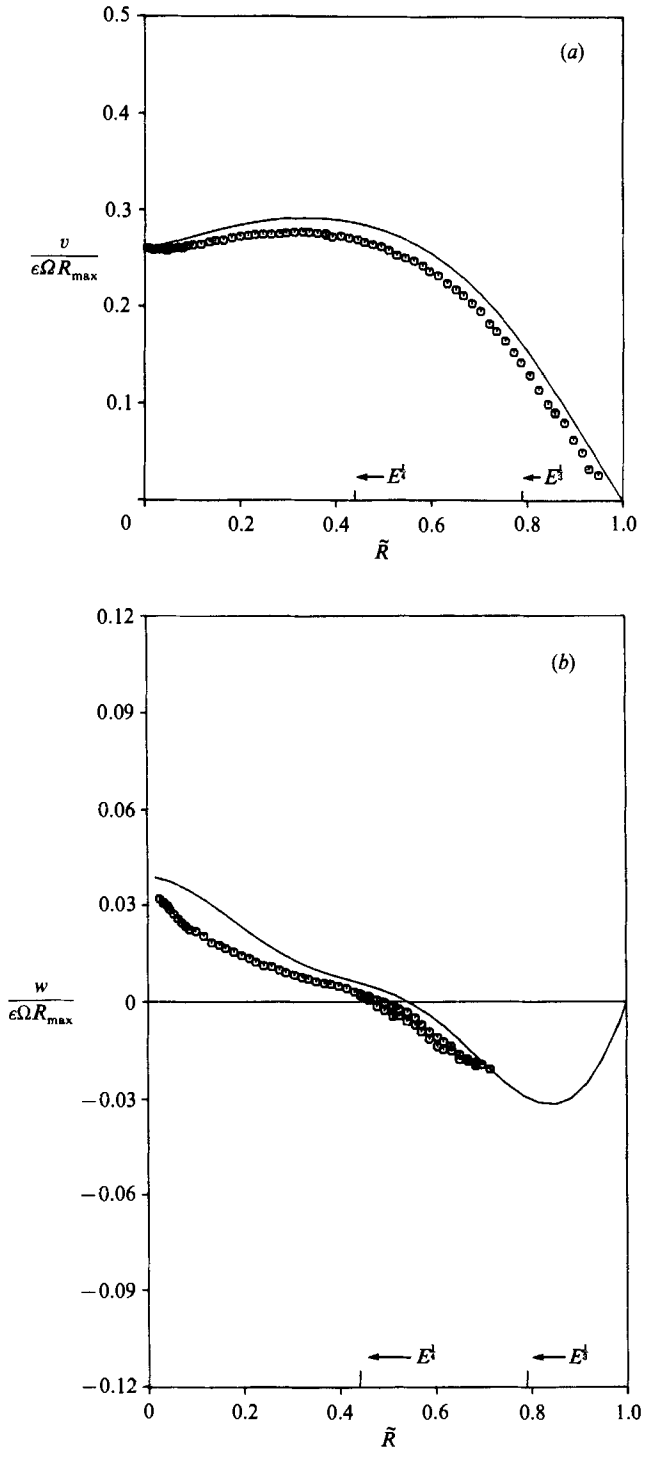

FIGURE 7. Measured and computed traverses for straight-walled rotor at $z = 0.55$ for Ekman number $= 10.9 \times 10^{-6}$, Rossby number $= 0.10$, Froude number $= 210$. Experimental data indicated by symbols; solid line indicates computed results at Froude number $= 210$. (*a*) Azimuthal velocity, (*b*) axial velocity.

rotor (figure 7*a*, *b*) show a marked contrast. A systematic error, probably corresponding to the second of the two causes discussed earlier (improper phase-angle variation), is evident here, but nevertheless the picture is seen to be quite different. The thicknesses seen are of order $E^{\frac{1}{3}}$ and $E^{\frac{1}{4}}$, and do not show the thinner modified $E^{\frac{1}{2}}$ layer seen with the slanted-wall rotor.

Measurements were also made for Rossby numbers of 0.20, 0.30, 0.40, and 0.50 at similar Ekman numbers. The azimuthal velocities (again non-dimensionalized by the peripheral speed of the disk in the rotating frame) were nearly the same in the outer 10% of the layer. However the value of the 'plateau' (see figures 4*a*, *b*) decreased from about 0.2 at a Rossby number of 0.10 to about 0.15 at a Rossby number of 0.50. Were nonlinear effects negligible through this whole range, these traverses would collapse to a single line. Similarly the axial velocities were similar near the wall, but were much attenuated away from the wall in the higher Rossby number cases. As pointed out earlier, at higher disk overspeeds (higher Rossby numbers) it was actually possible to see the free surface shape change as the disk overspeed was changed. Thus any analysis for these higher Rossby number cases would require a mechanism for moving the free surface as well as the inclusion of the nonlinear terms.

5. Conclusions

Both measured and computed results clearly show the modified $E^{\frac{1}{2}}$ layer along the slanted sidewall as predicted by the analysis. This is in contrast to the $E^{\frac{1}{3}}$ and $E^{\frac{1}{4}}$ layers seen with the vertical-walled cylinder. Trends with increasing Rossby number were measured, though not emphasized here.

The feasibility of using a laser-Doppler velocimeter in the rotor frame of reference in an incompressible fluid has been demonstrated. Data scatter has been greatly reduced from previous results taken in the laboratory frame. With due attention to alignment, quite accurate measurements of secondary flows were shown to be possible.

Good agreement was found with the results of a finite-difference simulation of the linearized governing equations. Using previous experience with strongly rotating flows, a robust, efficient solution algorithm on a boundary-fitted mesh was developed. Better agreement would be possible if the free surface shape were allowed to distort slightly with the solution rather than being fixed with the solid-body-rotation shape. This would require an adaptive mesh, but would be useful and necessary for the analysis of flows at higher Rossby numbers.

Support of this research by the US Department of Energy under contract DE-AC05-820R20900 is gratefully acknowledged.

REFERENCES

Beggs, G. O. 1984 Flow measurements in rotating fluids. M.S. thesis, University of Virginia.

Dongarra, J. J., Moler, C. B., Bunch, J. R. & Stewart, G. W. 1979 *Linpack User's Guide.* Philadelphia: SIAM.

Greenspan, H. P. 1968 *The Theory of Rotating Fluids.* Cambridge University Press.

Greenspan, H. P. 1982 Simulation of countercurrent flow in a gas centrifuge. *School of Engineering and Applied Science. University of Virginia, Rep.* UVA-ER-746-82U.

Harlow, F. H. & Welch, J. E. 1965 Numerical calculations of time-dependent viscous incompressible flow of fluid with a free surface. *Phys. Fluids* **8**, 2182–2189.

HEIJST, G. J. F. VAN 1986 Fluid flow in a partially-filled rotating cylinder. *J. Eng Math* **20**, 233–250.

HEUSER, G. E., RIBANDO, R. J. & WOOD, H. G. 1986 A numerical simulation of inertial waves in a rotating fluid. *Computer Meth. Appl Mech. Eng* **57**, 207–222.

HOGLUND, R. L., SHACTER, J. & VON HALLE, E. 1979 Diffusion separation methods. *Encyclopedia of Chemical Technology*, 7, 3rd edn Wiley.

MALISKA, C. R. & RAITHBY, G. D. 1984 A method for computing three dimensional flows using non-orthogonal boundary-fitted coordinates. *Intl J. Numer. Meth. Fluids* **4**, 519–537.

OLANDER, D. R. 1972 Technical basis of the gas centrifuge. *Adv. Nuclear Sci. Technol.* **6**, 105.

OSTRANDER, M. J. 1985 Elliptic grid generation. M.S. thesis, University of Virginia.

PALMER, J. L. 1987 Flow in a partially filled rotating tapered cylinder, M.S. thesis, University of Virginia.

PATEL, N. R. & BRIGGS, D. G. 1983 A MAC scheme in boundary-fitted curvilinear coordinates. *Numer. Heat Transfer* **6**, 383–394.

POPP, C. G. 1987 Countercurrent velocity measurements from the rotating frame of reference. M.S. thesis, University of Virginia.

RIBANDO, R. J. & SHADDAY, M. A. 1984 The Ekman matching condition in a partially filled rapidly rotating cylinder. *J. Comp. Phys.* **53**, 266–288.

SHADDAY, M. A. 1982 Flow in a partially filled rotating cylinder. Ph.D. thesis, University of Virginia.

SHADDAY, M. A., RIBANDO, R. J. & KAUZLARICH, J. J. 1983 Flow of an incompressible fluid in a partially filled rapidly rotating cylinder with a differentially rotating cylinder. *J. Fluid Mech.* **130**, 203–218.

SMITH, J. C. 1983 Axial flow in a tapered wall centrifuge. B.S. thesis, University of Virginia.

TOKOI, H., OZAKI, N. & HARADA, I. 1980 Measurements of velocity profiles of gas in a rapidly rotating cylinder. *Rev. Sci. Instrum.* **51**, 1318–1322.